Surface Tension Driven Water Strider Robot using Circular Footpads

Onur Ozcan*, Han Wang*, Jonathan D. Taylor, and Metin Sitti

Carnegie Mellon University, Department of Mechanical Engineering, Pittsburgh, PA, USA

Abstract— **Water strider insects have attracted many researchers' attention with their power efficient and agile water surface locomotion. This study proposes a new water strider insect inspired robot, called STRIDE II, which uses new circular footpads for high lift, stability, payload capability, and a new elliptical leg rotation mechanism for more efficient water surface propulsion. The lift, drag and propulsion forces and the energy efficiency of this robot are modeled and experiments are conducted to verify these models. A maximum lift capacity of 53 grams is achieved with a total of 12 footpads, each 4.2 cm in diameter for a robot weighing 21.75 grams. For this robot, a propulsion efficiency of 22.3% is measured. Maximum forward and turning speeds of the robot are measured as 71.5 mm/sec and 0.21 rad/sec, respectively. These water strider robots could be used in water surface monitoring, cleaning, and analysis in lakes, dams, rivers and sea.**

Index Terms— **Biologically Inspired Robots, Mobile Robotics, Surface Tension, Miniature Robots.**

I. Introduction

Researchers have recently focused on the surface-tension-driven locomotion of water-walking arthropods such as water striders and fisher spiders [1], [2], [3], [4], [5], [6]. The theory behind their lift, propulsion and drag mechanisms have been revealed and enabled the development of various robotic counterparts of these water-walking arthropods. Being inspired by these insects, there have been several studies to design and manufacture bio-inspired legged robots to achieve power efficient, fast, silent, and stable legged locomotion on deep or very shallow water surfaces. Hu *et al.* [3] proposed a mechanical water strider powered by an elastic thread. Suhr *et al.* [7] developed a controllable water strider robot utilizing three piezoelectric unimorph actuators. Song *et al.* [8], [9] studied the numerical modeling of the supporting legs by respectively developing a rigid-leg model and a compliant-leg model, and built a non-tethered water strider robot with two miniature DC motors and a lithium polymer battery. Suzuki *et al.* [10] showed two water strider robots with hydrophobic microstructures on the surface of the supporting legs respectively driven by a vibration motor and a slider-crank mechanism. Shin *et al.* [11] developed a water jumping robot that is able to achieve a vertical jumping motion on the water surface with a latch mechanism driven by a shape memory alloy actuator.

In this work, to achieve an efficient and fast legged propulsion, a new improved water strider robot called STRIDE II using a DC motor actuated four-bar elliptical leg rotation mechanism for water propulsion is proposed. This robot has concentric circular footpads that are designed, analyzed, and manufactured using laser cutting to generate more lift force per unit area and greater stability when compared to STRIDE [9]. Moreover, the drag force model of the supporting structure and the propulsion mechanism are investigated and explained in detail. Finally, the robustness and the payload capacity are improved with the new design while keeping the features like silent operation, little subsurface disturbance, and maneuvering capabilities in both deep and shallow water of the older version, STRIDE [9].

II. Problem Statement

Water strider insect locomotion exemplifies robust and efficient water surface walking because of the lift force mechanism, low drag force on supporting legs, and the elliptical trajectory of the propelling legs. Therefore, these three features should be captured in the design of a water strider inspired robot.

The lift force mechanism that a water strider insect dominantly uses is the surface tension force of water that is linearly proportional to the length of the supporting legs. Since the weight of the insect scales with its volume, if its size is smaller, the surface tension force is used as the lift force mechanism instead of buoyancy. To mimic the water strider insect, the robot should use surface tension as the dominant part of the lift force; therefore, the robot should have a relatively low weight and small size but long legs to support itself on water. The water strider robot should also have enough payload capacity to carry on-board electronics, power supply, actuators, and sensors for control, autonomous locomotion, and potential future applications like monitoring water quality. On the other hand, for a robot to have a high payload capacity using surface tension, the required leg lengths might be unrealistically long. Therefore, the supporting structures are designed as concentric circular footpads, which increase the total length subjected to lift force while keeping the total area of the supporting structures relatively small. The lift force mechanism and the results are explained in detail in section III.

The drag forces that a water strider insect experiences are relatively low at the supporting legs, enabling them to move rapidly and efficiently on the water's surface. This is due to the lift force mechanism of a water strider, which does not require the insect to break the water surface to stay afloat. Therefore, in order to claim that the designed robot is efficient for water surface locomotion, the drag force model for the robot should be established, which is explained in detail in section IV.

---

*These authors contributed equally to this work.

In addition to the problems about lift force generation and drag force modeling, the propulsion mechanism of the robot should be designed so that the drag forces on the propelling legs, which are propulsion forces for the robot due to the momentum transfer principle [5], move the robot quickly. It is desired to mimic a water strider insect, which moves its propelling legs in an elliptical trajectory to efficiently increase the propulsion forces. Agility of the robot, complexity, and availability of parts that are used in propulsion mechanism should also be considered. Within these considerations, the final design of STRIDE II is shown in Fig. 1.
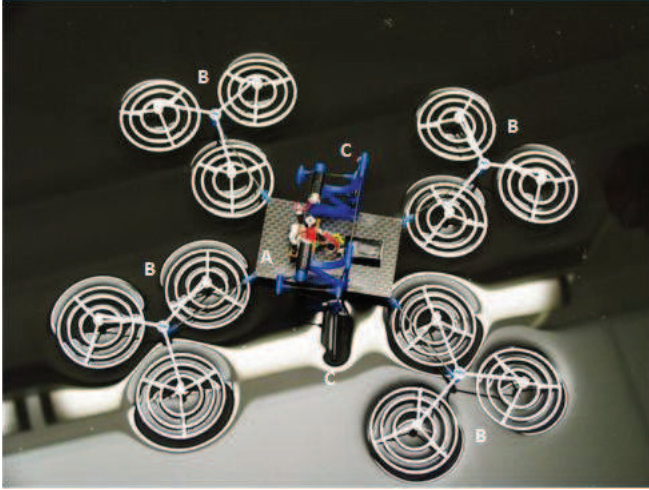

Fig. 1. Photograph of STRIDE II: **A**: The robot body with a control board, a battery, and two four-bar actuators; **B**: Four sets of circular concentric supporting footpads. **C**: Two propulsion legs with elliptical rotation trajectory, driven by two DC motors.

III. LIFT FORCE ANALYSIS AND EXPERIMENTS

In this section, a numerical model of the water surface near a partially submerged rigid cylinder, proposed before in [8] is used to develop a model for supporting footpads that consist of concentric circles as a new footpad geometry.

A. 2-D Modeling

To simulate the lift force for a circular footpad, first the cross-section of a footpad, which will be considered as a pattern with several circles submerged in water as shown in Fig. 2, needs to be investigated using the models proposed in [8]. The number of circles that are submerged is equal to the number of concentric circles in the footpad.

The weight of the water displaced by the footpad is identical to the amount of lift force the footpad generates. In other words, the weight of the water required the fill the volume bounded above by an undisturbed water surface ($z = 0$ line) and bounded below by the water-air interface is equal to the integral of the areas A_b and A_{st} along the 3-D footpad geometry, and is the total lift force. The buoyancy component and the surface tension component of the lift force are proportional to A_b and A_{st}, respectively [8], [11]. The shape of the air-water interface in the disturbed case is governed by the Young-Laplace equation [8]. After
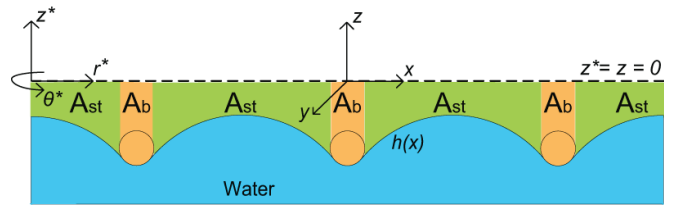

Fig. 2. Side cross-section view of a three concentric-circle footpad. Areas A_b and A_{st} represent the areas that the footpad is deforming because of its weight and the footpad is deforming because of the hydrophobicity of the leg material, respectively.

calculating the surface profile, the total lift force is calculated by integrating the profile around the center of the footpad.

Similar to the model in [8], the 2-D water surface profile analysis of a cross-section forms the basis of the concentric footpad lift force calculation. The basic differences are the profile interference due to nearby concentric circles and the change of the coordinate system from cartesian to polar coordinates. To begin the calculations, an $h(x)$ profile is created using the 2-D analysis in [8]. The radius of the material is specified here and a specific $h(x)$ is created by solving the Young-Laplace equation. Next, this profile is modified for several numbers of concentric circles. The concentric circle radii are compared with pre-defined "infinity" (the distance where the water surface depth reaches its original value, i.e. the dimple disappears, and is estimated as 1 cm using [8] and observations), and the interferences are calculated. A new modified $h(x)$ is created for given number of concentric circles. Figure 3 shows the water surface profile calculated for a footpad that consists of 5 concentric circles with 4, 9, 13, 17 and 21 mm radii, respectively.
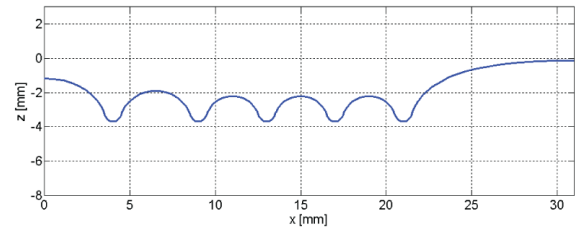

Fig. 3. The simulation result of the water surface profile $h(x)$ for a footpad with five concentric cirles with radii of 4, 9, 13, 17 and 21 mm.

B. 3-D Modeling

The modified water surface profile consists of data from the center of the concentric footpad to the outer undisturbed surface. This modified surface should be integrated along the footpad in order to find the lift forces. A coordinate system transformation is conducted in order to take the integral around the center of the footpad. Figure 2 shows how this transformation is carried out.

The polar coordinate system, (r^*, θ^*, z^*), where the integral for the lift force of footpad will be calculated is placed at the center of the footpad as shown in Fig. 2. $z = 0$ is undisturbed water surface. Since the water surface profile changes only with the distance from the center of the footpad, $h(x)$ will be directly transformed to $h(r)$. Following the coordinate system transformation, a polar integral around the center of the footpad is performed to calculate the total amount of lift force produced by the footpad:

$$F_{lift} = \int_0^{2\pi} \int_0^{r+\infty} r h(r) dr d\theta \qquad (1)$$

To find the buoyancy component of the lift force separately, the area A_b should be integrated, therefore the limits of the r integral should be changed. Similarly, for the surface tension component of the lift force, only the area A_t should be considered and the limits of the r integral should be adjusted appropriately.

C. Simulation and Experimental Lift Results

The simulation results are calculated using the model described above and the experimental results are obtained by loading a single footpad with a platform that can carry a load. Several grams of sugar are placed on the platform above the footpad and the amount of weight that it can carry just before breaking the water surface and sinking is measured.

For the experiments, four different footpads with different numbers of concentric circles and diameters are tried (8-42 mm, 14-42 mm, 8-26-42 mm, 20-32-42 mm). The diameter of the outer concentric circle is kept at 42 mm to keep the area bounded. The dimensions for these footpads are found by running simulations to maximize different parameters (Surface Tension/Buoyancy, Surface Tension, Total Lift x Surface Tension/Buoyancy and Total Lift, respectively). The simulation and experiment results are shown in Table I. The results show the simulated lift force values are close to the experimental ones except the last footpad with 3 concentric circles with diameters 20-32-42 mm. The simulation assumes the cross-sections of footpads are circular, but in reality, the cross-sections are rectangular. The sharp edges at the ends of the rectangles may break the water surface before the maximum lift force is achieved. We believe this factor is the reason for the overestimation in the last row of Table I.

TABLE I
SIMULATION AND EXPERIMENTAL LIFT FORCE RESULTS

Concen. Circle Diameters (mm)	Simulated Lift (mN)	Mean Exp. Lift (mN)	Standard Deviation (mN)
8-42	81.2	85.6	5.4
10-26-42	116.1	111.5	8.5
14-42	93.9	91.3	7.2
20-32-42	141.8	129.7	7.6

D. Optimal Footpad Design

The footpad with diameters 20-32-42 mm is chosen to be the best design since it maximizes the lift force, which is the most significant quantity to be optimized. The total lift capacity of a 12 footpad robot would therefore be approximately 53 grams, more than necessary to carry onboard electronics, a 3.5 Volt battery, two miniature DC motors, and two leg rotation mechanisms, which weighs 21.75 grams, with a safety factor of approximately 2. Hence, the extra payload capacity of the robot is 31.25 grams.

The simulation results in [8] show that surface tension based lift force is directly correlated to the contact angle of the supporting leg material. However, the advantage of being hydrophobic diminishes for contact angles above 120 degrees, above which the lift force is approximately the same for any angle. Therefore, the footpads are coated with a hydrophobic coating (Cytonix, WX2100) with a contact angle of 145 degrees to obtain the best available surface tension force. The hydrophobicity of the leg enables us to maximize the lift force for a given geometry. This contact angle of 145 degrees is used in the simulations.

IV. ANALYSIS AND EXPERIMENTS ON ROBOT DYNAMICS

When the robot is translating on water, the equation of motion can be written as:

$$F_P - F_R = ma \qquad (2)$$

where m is the mass of the robot, a is its acceleration, F_P is the propulsion force on the robot, which arises from the drag forces acting on the two rowing wire-legs when they are driven backwards against the water with respect to the robot body, and F_R is the resistance force which consists of various drag forces acting on the supporting footpads. When these two forces equal to each other, the robot achieves its terminal velocity.

A. Resistance Force Analysis

Three physical mechanisms are potentially responsible for the drag forces acting on the robot:

1) Capillary-Gravity Wave Drag: Any partially submerged body moving at the water surface with a velocity greater than $c_{min} = (4g\gamma/\rho)^{1}/4 \approx 0.23$ m/s, the minimum phase velocity of surface waves, will generate capillary-gravity waves that dissipate energy and resist the body's motion. Here, g is the gravity, γ is the surface tension, and ρ is the density of water.

2) Surface Tension Drag: When a partially submerged body is at rest on the water surface, the surface tension forces acting on the two contact lines on each side of the body are symmetric, and there is no horizontal resultant force. However, when the body moves, asymmetry of the surface tension forces occurs and the resultant force creates the surface tension drag.

3) Hydrodynamic Drag: A moving partially submerged body creates a viscous drag which consists of a normal pressure component (form drag), a shear stress component (skin friction drag), and a trailing vortex wake component (interference drag). These three drag forces act over the whole of the submerged section of the body.

In the case of STRIDE II, the estimated velocity of the robot is well below c_{min}, thus the capillary-gravity wave drag is not expected to contribute to the overall resistance to the robot's motion. In [12], it is shown that the maximum surface tension drag achieved before meeting water surface breaking conditions is significantly less than the hydrodynamic drag. Therefore, it is asserted that hydrodynamic drag dominates the lateral resistance force on the robot.

The hydrodynamic drag is given as:

$$D_H = 1/2\rho A C_D U^2 \qquad (3)$$

where ρ is the density of water, A is the reference area, C_D is the drag coefficient including all contributions from the

form drag, the skin friction drag, and the interference drag, and U is the velocity of the robot with respect to the water. It is known that C_D varies as a function of the Reynolds number, R_e, of the object [13], which generally combines the fluid properties of density and viscosity, as well as the object's velocity and characteristic length. Although R_e, and thus C_D, can vary greatly, the variation within a practical range of interest is usually small, so that C_D is often treated as a constant [14]. Usually, Eq. (3) is applicable with C_D as a constant when $R_e > 1000$.

It is worth noting that C_D is always associated with a particular surface area, A [15]. Here, this area is defined as the orthographic projection of the dimple's frontal area on a plane perpendicular to the direction of motion, which is:

$$A = hl \qquad (4)$$

for the cylindirical wire-legs, where h is the dimple depth and l is the lenght of the wire-legs; or

$$A = \sum_i h(D_i + d_i) \qquad (5)$$

for the footpads, where D_i and d_i are the outer and inner diameters of each concentric circle of the footpads, respectively. Figure 4 shows the defined reference areas of a cylindrical wire-leg and a footpad with three concentric circles.

Note that the hydrodynamic drag has a simple quadratic relationship with U^2. In next section, experiments are performed to show the existence of this relationship and thus demonstrate the dominance of the hydrodynamic drag.

B. Footpad Drag Coefficient Measurement Results

As mentioned earlier, when the robot is in motion, the drag coefficient C_D stays constant if $R_e > 1000$. Experiments are performed to measure this constant value of C_D.

A passive robot platform with four sets of supporting footpads is built to conduct the experiments. In each experiment, an initial velocity is applied to the platform, and its displacement with respect to time is measured using a video tracking technique, shown in Fig. 5(a). The results were then used to obtain the mean velocity and acceleration information by calculating the first and the second derivatives, in which the Savitzky-Golay filters were applied to smooth the data [16]. Figure 5(b) illustrates the experimental data acceleration with respect to velocity. The matching performance of quadratic curve fitting implies a quadratic relationship between the acceleration and the velocity. Therefore, according to Eq. (3), it is reasonable to assert that the hydrodynamic drag serves as the primary resistance force for the footpads.
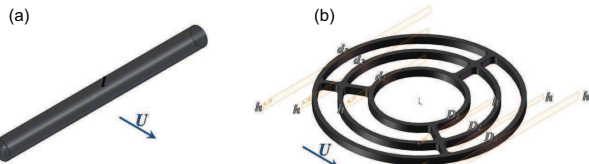
Fig. 4.   **(a)** Schematics of the defined reference area of a cylindrical wire-leg: $A = hl$; **(b)** Schematic of the defined reference area of a footpad with three concentric circles: $A = \sum_i h(D_i + d_i)$. U denotes the direction of velocity of the wire-leg or the footpad.

Since, in the experiments, no propulsion force is applied to the platform and hydrodynamic drag is considered to be the only source of resistance, substitute Eq. (3) into Eq. (2):

$$ma = F_D = 1/2\rho A C_D U^2 \qquad (6)$$

Thus:

$$C_D = \frac{2ma}{\rho A U^2} \qquad (7)$$

Given a from the experimental data and A calculated using Eq. (5), C_D can be directly computed. Figure 6 shows the variance of C_D with respect to R_e. It is shown that C_D varies slightly in the experimental velocity range (corresponding R_e range: $1671 - 2833$) which overlaps with the estimated velocity range of the robot. Therefore, 0.155 is chosen as an estimated value of the drag coefficient for the supporting footpads.
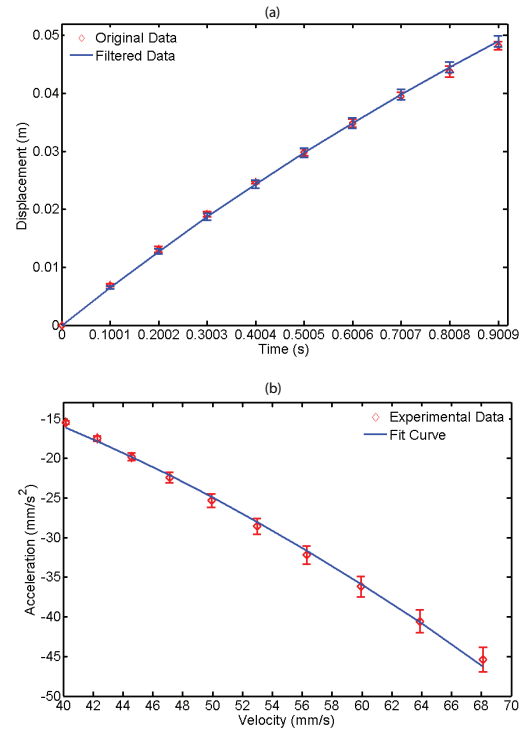
Fig. 5.   **(a)** Plot of experimental displacement data with respect to time. Savitzky-Golay filters were applied to smoothen the data. **(b)** Plot of experimental data of acceleration with respect to the velocity. The fitting model is $y = ax^2$ and the R-square value of the fit is 0.9974. This quadratic relationship justifies the dominance of the hydrodynamic drag in the resistance forces of the footpads.

C. Robot Terminal Velocity Estimation

As discussed before, the calculation of the resistance force of the robot, F_R, in Eq. (2) becomes fairly simple based on Eq. (7) and the experimental evaluation of C_D. But the analysis of the propulsion force, F_P, remains less clear, as the operating range of the rowing wire-legs' velocity is measured to range from 250 mm/s to 755 mm/s, which has exceeded $c_{min} \approx 0.23$ m/s. This fact implies that the capillary-gravity wave drag may become one of the sources of F_P. However, Bush $et\ al.$ [5] conducted experiments with high-speed video and particle-tracking and concluded that the water striders transfer momentum to the underlying fluid
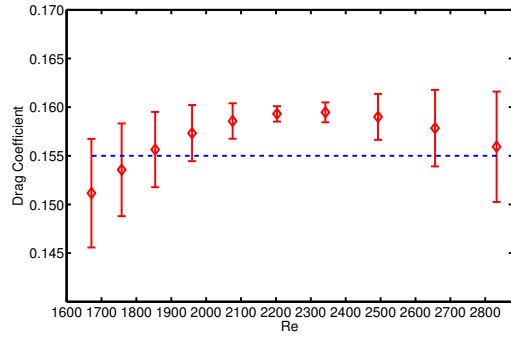
Fig. 6. Plot of experimental drag coefficient with respect to Reynolds number. 0.155 is chosen to be an estimate of the drag coefficient for the supporting footpads of STRIDE II.

not primarily through capillary waves, but rather through hemispherical vortices shed by their rowing legs.

To obtain knowledge of the terminal velocity of the robot, a hydrodynamic drag force of a general form $D = 1/2\rho A C_D U^2$ is assumed to act as F_P, where A is calculated as in Eq. (4) and C_D is chosen as 0.09, an experimental drag coefficient for a half streamlined body [13], which closely resembles the shape of the dimple associated with the wire-legs. Let a in Eq. (2) set to be zero, and substitute the expressions of F_P and F_R into 2:

$$1/2\rho A_w C_{Dw} U_w^2 - 1/2\rho A_f C_{Df} U_t^2 = 0 \tag{8}$$

where U_w is the velocity of the rowing wire-legs with respect to the robot body, U_t is the terminal velocity of the robot, A_w and A_f are the reference areas of the wire-legs and the footpads, respectively, and C_{Dw} and C_{Df} are the drag coefficients of the wire-legs and the footpads, respectively. Equation (8) can be rearranged as:

$$U_t = \sqrt{\frac{A_w C_{Dw}}{A_f C_{Df}}} U_w \tag{9}$$

Since A_w and A_f can be calculated using Eq. (4) and Eq. (5), and C_{Dw} and C_{Df} are respectively determined as 0.09 and 0.155, a quantitative relationship between U_t and U_w can be obtained:

$$U_t = 0.103 U_w \tag{10}$$

Using this equation, the terminal velocity of the robot can be estimated, given the velocity of the rowing wire-legs which can be further calculated from the gearmotors' speed; a controllable parameter.

D. Terminal Velocity Experiments

Experiments were performed to acquire velocity data of the robot and the wire-legs. By top-view video observation, the motor speed was first measured, and then was used to calculate U_w. U_t was directly obtained by video tracking. Table II shows all data from five different measurements, from which an approximate agreement to Eq. (10) is revealed. These experiments are able to justify the conclusion of Bush et al. [5] that capillary waves do not play an essential role in the propulsion, although the waves are still observable due to the rowing action.

TABLE II
COMPARISONS BETWEEN EXPERIMENTAL U_t AND U_w VALUES

Exp. #	U_w (mm/s)	U_t (mm/s)	U_t/U_w
1	286.1	28.6	0.1000
2	304.5	32.9	0.1080
3	507.9	48.9	0.0963
4	592.6	53.3	0.0899
5	617.7	59.1	0.0957
6	742.5	71.5	0.0963

V. ROBOT FABRICATION AND EXPERIMENTS

A. Robot Fabrication

1) Footpads: The footpads are cut using a laser engraver (GCC, Venus) from a 1 mm thick Delrin sheet, and then coated with super-hydrophobic material fluorothane (Cytonix, WX2100). Assembly is done by gluing.

2) Actuators: The frame and all the joint parts of the actuating mechanism are fabricated using a rapid prototyping machine (3D Systems, Inc., Invision HR). The 20 mm long rowing wire-legs are formed by Teflon coated stainless steel wires (diameter: 0.33 mm). The fabricated actuating mechanism including the gearmotor weighs around 2.9 grams. The four-bar mechanism, its dimensions and the elliptical-like trajectory is shown in Fig. 7.
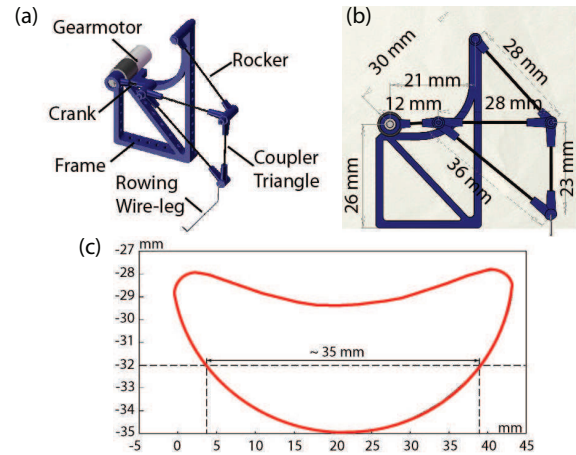

Fig. 7. **(a)** Sketch of the four-bar actuating mechanism with a miniature gearmotor. **(b)** Significant dimensions of the four-bar actuator. **(c)** Simulation of the trajectory of the rowing wire-leg. The origin is fixed at the locus of the gearmotor.

3) Robot Body: Two four-bar actuators with miniature gearmotors (Precision Microdrives, 206-101), a custom control board, and a polymer Li-Ion battery (Powerizer, PL-651628-2C) take up the most weight of the robot body. A 70 mm x 44 mm x 1 mm carbon fiber sheet is used as the main body of the robot. Figure 1 shows the fabricated STRIDE II, which weighs 21.75 grams.

4) On-board Electronics: To achieve more effective control, a custom control board is developed for STRIDE II. It includes a microcontroller (Microchip, PIC18LF2520), a motor driver (Freescale, MPC17C724), a voltage regulator (Analogic, AAT3221), an IR receiver (Vishay, TSOP36236), a timer (ST TS555), a trimming potentiometer (Bourns, 3223), and several resistors and capacitors. It is capable of power management, motor control, and IR communication.

B. Robot Experiments

The robot is controlled by using an IR remote. Figures 8(a) and 8(b) respectively show a forward linear motion and a right-turning motion of the robot with speeds of 71.5 mm/s and 0.21 rad/s. No feedback control is applied; voltage values for the motors that enable the robot to move in a straight line or with a predefined curvature are tuned beforehand. Attached video shows the operation of the robot.

Robot power consumption and efficiency are calculated and shown in Table III. Here, the motor efficiency is taken into consideration to obtain the input mechanical power to the actuators. Therefore, the calculated robot efficiency is based on the input mechanical power and output mechanical power rather than the input electrical power. The motors used have a fairly low efficiency, leading to excess power usage. This can be improved by using higher efficiency, lightweight motors. It is noted that the input and output mechanical power are on the order of microwatts, which implies this robot can be operated at very low power.
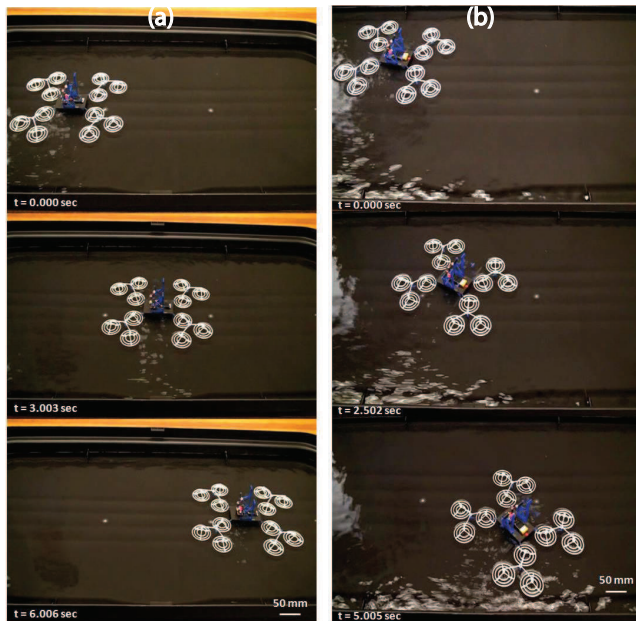

Fig. 8. Photo snapshots of STRIDE II in motion **(a)** Forward linear motion at a speed of 71.5 mm/s. **(b)** Right turn at an angular speed of 0.21 rad/s.

TABLE III

Exp. Robot Power Consumption and Efficiency Results

Robot Speed (mm/s)	Input Mech. Power (μW)	Output Mech. Power (μW)	Robot Efficiency
28.6	38.08	7.903	20.8%
32.9	53.92	12.03	22.3%
48.9	320.0	39.50	12.3%
53.3	319.6	51.16	16.0%
59.1	428.4	69.74	16.3%
71.5	641.5	123.6	19.3%

VI. Conclusion

In this paper, the STRIDE II robot, using concentric circular footpads and elliptically rotating propelling legs is analysed and developed. The robostness of the robot is enhanced when compared to the previous water strider robots,

its lift force model is established and dynamic forces like drag and the propulsion force that STRIDE II experiences are modeled. The use of concentric circular footpads as the supporting structure increased the payload capacity of the robot by a factor of 4. Two DC motors with four-bar mechanisms are used for propulsion, enabling the propelling leg to have an elliptical trajectory which supplies more propulsion force compared to a circular trajectory. The static and dynamic forces applied on the robot body are investigated and models for the forces that the robot experiences are established and supported with experimental data.

Autonomous control of single and multiple water strider robots is the next planned step. In the future, this robot can be used as an educational or toy robot, or swarm of these robots can be used for varius applications such as water quality monitoring on dams, lakes or seas.

References

[1] M. W. Denny, *Air and Water: The Biology and Physics of Lifes Media*. Princeton, NJ: Princeton University Press, 1993.

[2] R. B. Suter, O. Rosenberg, S. Loeb, H. Wildman, and J. H. J. Long, "Locomotion on the water surface: Propulsive mechanisms of the fisher spider dolomes triton," *Journal of Experimental Biology*, vol. 200, pp. 2523–2538, 1997.

[3] D. L. Hu, B. Chan, and J. W. M. Bush, "The hydrodynamics of water strider locomotion," *Nature*, vol. 424, pp. 663–666, 2003.

[4] X. Gao and L. Jiang, "Water-repellent legs of water striders," *Nature*, vol. 432, p. 36, 2004.

[5] J. W. M. Bush and D. L. Hu, "Walking on water: Biolocomotion at the interface," *Annual Review of Fluid Mechanics*, vol. 38, pp. 339–369, 2006.

[6] D. Vella and P. D. Metcalfe, "Surface tension dominated impact," *Physics of Fluids*, vol. 19, pp. 072 108–1–11, 2007.

[7] S. H. Suhr, Y. S. Song, S. J. Lee, and M. Sitti, "Biologically inspired miniature water strider robot," in *Proceedings of Robotics: Science and Systems I*, 2005, pp. 319–325.

[8] Y. S. Song, S. H. Suhr, and M. Sitti, "Modeling of the supporting legs for designing biomimetic water strider robots," in *Proceedings of IEEE International Conference on Robotics and Automation*, 2006, pp. 2303–2310.

[9] Y. S. Song and M. Sitti, "Stride: A highly maneuverable and non-tethered water strider robot," in *Proceedings of IEEE International Conference on Robotics and Automation*, 2007, pp. 980–984.

[10] K. Suzuki, H. Takanobu, K. Noya, H. Koike, and H. Miura, "Water strider robots with microfabricated hydrophobic legs," in *Proceedings of the IEEE/RSJ International Conference on Intelligent Robots and Systems*, 2007, pp. 590–595.

[11] B. Shin, H. Y. Kim, and K. J. Cho, "Towards a biologically inspired small-scale water jumping robot," in *Proceedings of the 2nd Biennial IEEE/RAS-EMBS International Conference on Biomedical Robotics and Biomechatronics*, 2008, pp. 127–131.

[12] Y. S. Song and M. Sitti, "Surface-tension-driven biologically inspired water strider robots: Theory and experiments," *IEEE Transactions on Robotics*, vol. 23, pp. 578–589, 2007.

[13] S. Vogel, *Life in Moving Fluids*, 2nd ed. Princeton, NJ: Princeton University Press, 1994.

[14] L. J. Clancy, *Aerodynamics*. London: Pitman Publishing Limited, 1975.

[15] B. W. McCormick, *Aerodynamics, Aeronautics, and Flight Mechanics*. New York, NJ: John Wiley & Sons, Inc., 1979.

[16] J. Luo, K. Ying, P. He, and J. Bai, "Properties of savitzky-golay digital differentiators," *Digital Signal Processing*, vol. 15, pp. 122 – 136, 2005.